The broadening of Lyman-α forest absorption lines

Antonella Garzilli,[1][*] Tom Theuns[2] and Joop Schaye[3]

[1]*Lorentz Institute, Leiden University, Niels Bohrweg 2, Leiden, NL-2333 CA, the Netherlands*
[2]*Institute for Computational Cosmology, Department of Physics, Durham University, DH1 3LE Durham, UK*
[3]*Leiden Observatory, Leiden University, PO Box 9513, 2300 RA Leiden, the Netherlands*

ABSTRACT

We provide an analytical description of the line broadening of H I absorbers in the Lyman-α forest resulting from Doppler broadening and Jeans smoothing. We demonstrate that our relation captures the dependence of the line width on column density for narrow lines in $z \sim 3$ mock spectra remarkably well. Broad lines at a given column density arise when the underlying density structure is more complex, and such clustering is not captured by our model. Our understanding of the line broadening opens the way to a new method to characterize the thermal state of the intergalactic medium and to determine the sizes of the absorbing structures.

Key words: intergalactic medium – quasars: absorption lines – large-scale structure of Universe.

1 INTRODUCTION

The intergalactic medium (IGM) is detected as intervening absorption in the spectra of background sources (Gunn & Peterson 1965), in the form of a 'forest' of H I (Lynds 1971; Weymann, Carswell & Smith 1981, see e.g. Rauch 1998 for a review) and He II (Jakobsen et al. 1994; Davidsen, Kriss & Zheng 1996) absorption lines. This gas is very highly ionized, $x = n_{\rm H I}/n_{\rm H} \sim 10^{-4}$, by a pervasive background of ionizing radiation produced by galaxies and quasars (Haardt & Madau 1996), with hints of an increasingly neutral fraction, $x \sim 0.1$, above redshift $z \sim 7$ (Mortlock et al. 2011). At all times, it contains the majority of baryons (Fukugita, Hogan & Peebles 1998).

The growth of structure in a cold dark matter (CDM) Universe naturally gives rise to a 'cosmic web' of voids, sheets and filaments, with absorbers arising when the sight-line intersects higher density regions, as demonstrated in analytic models (Bi & Davidsen 1997; Schaye 2001) and simulations (Cen et al. 1994; Weinberg et al. 1996; Theuns et al. 1998). The temperature of this gas is set by the balance between photoheating and adiabatic expansion and compression, resulting in a well-defined temperature–density relation, $T = T_0(\rho/\langle\rho\rangle)^{\gamma-1}$, where $\gamma \approx 1$ immediately after reionization, and $\gamma \rightarrow 1 + 1/1.7$ asymptotically long after reionization (Hui & Gnedin 1997; Theuns et al. 1998). Patchy reionization of either H I or He II may lead to patchy photoheating (Abel & Haehnelt 1999; McQuinn et al. 2009) and hence spatial fluctuations in the temperature, but these have not (yet) been detected (Theuns et al. 2002a; McQuinn et al. 2011).

Feedback from star formation is an essential ingredient in models of galaxy formation and might impact the IGM (Theuns, Mo & Schaye 2001). For example, elements synthesized in stars are detected in the IGM (Cowie et al. 1995), even at low densities (Schaye et al. 2003). If, as is likely, this enrichment is due to galactic winds, then the IGM might not be ideal for making *cosmological* inferences. Fortunately, it appears that the effects of such winds are relatively small (Theuns et al. 2002c; McDonald et al. 2005; Viel, Schaye & Booth 2013). However, current simulations still struggle somewhat to reproduce the detected enrichment patterns as a function of density (Aguirre & Schaye 2005; Wiersma et al. 2010; Wiersma, Schaye & Theuns 2011) and hence may underestimate the effects of galaxy formation on the IGM.

Accurate measurements of the evolution of T_0 and γ are interesting, since they could constrain the epoch of H I and He II reionization (Theuns et al. 2002b), but also because the formation of small galaxies is quenched due to a reduction of atomic cooling (Efstathiou 1992) following reionization, and because photoheating evaporates the gas out of shallow dark matter potentials (Okamoto, Gao & Theuns 2008). This is a crucial ingredient in models of galaxy formation, in particular for dwarf galaxies and satellites (Benson et al. 2002; Sawala et al. 2014). The thermal state of the IGM is also an important 'nuisance' factor when using the Lyman-α forest to study the nature of the dark matter (Boyarsky et al. 2009), or to determine the amplitude of the UV-background (Bolton et al. 2005).

Schaye et al. (1999) described a method for inferring (T_0, γ) from the line width versus column density ($b-N_{\rm H I}$) scatter plot of Lyman-α lines, when the Lyman-α forest is fitted as a sum of Voigt profiles for example using VPFIT.[1] This improved and extended the work of Theuns et al. (1998) who had noted that the small b cut-off of the b-parameter distribution was sensitive to temperature.

---

[1] VPFIT is developed by R. Carswell and J. Webb, http://www.ast.cam.ac.uk/rfc/vpfit.html.

[*] E-mail: garzilli@lorentz.leidenuniv.nl

Schaye et al. (2000), and Ricotti, Gnedin & Shull (2000), Bryan & Machacek (2000) and McDonald et al. (2001) used this to measure the T–ρ relation at redshifts $z \sim 2$–4.

Since then other measurements have been performed over a larger redshift range, some also based on Voigt profile fitting (Rudie, Steidel & Pettini 2012), or based on small-scale power spectrum or wavelet analysis (Theuns & Zaroubi 2000; McDonald et al. 2000; Zaldarriaga, Hui & Tegmark 2001; Theuns et al. 2002b; Viel, Bolton & Haehnelt 2009; Lidz et al. 2010; Garzilli et al. 2012), transmission PDF statistics (Bolton et al. 2008; Viel et al. 2009; Calura et al. 2012; Garzilli et al. 2012) and more recently on curvature statistics (Becker et al. 2011). Current measurements still have large error bars for T_0 and constraints are even poorer for γ. Bolton et al. (2008) and Viel et al. (2009) even argue that $\gamma < 1$, which is difficult to understand from a theoretical point of view (McQuinn et al. 2009; Compostella, Cantalupo & Porciani 2013).

The basis for all these methods is the assumption that line widths are relatively directly related to the temperature of the absorbing gas. However, it is in fact well known that – in the simulations – the absorption lines are invariably wider than just the thermal broadening. In addition, there is a very large *scatter* in line widths at a given density, in the sense that some lines are *much* wider than the thermal width at a given density.

In this paper, we present a new model for measuring and interpreting line widths, which builds on previous work. In our model, lines are *always* broader than the thermal width, and we also explain the origin of the large scatter. We describe how the model can be used to infer not just T_0 and γ, but also to constrain the size of the absorbers. This paper is organized as follows. In Section 2, we begin by contrasting the 'fluctuating Gunn–Peterson' description of the IGM with one where the absorption is due to a distribution of individual absorbers. We do so in order to establish notation and explain the motivation for our modelling. We discuss the properties of these absorbers, and in particular what sets their line widths. In Section 3, we introduce the simulations and use them to test the basic assumptions of the model. In Section 4, we examine whether the method can in principle be applied to observables. We present a summary of our conclusions in Section 5.

2 LYMAN-α SCATTERING IN THE IGM

A Lyman-α photon has a large cross-section for exciting an H I atom from the ground state to the electronic $n = 2$ level. When the atom falls back to the ground state, the photon is in general not re-emitted in the same direction. This scattering of Lyman-α photons out of the sight-line to a source is usually called Lyman-α 'absorption' and is quantified by the optical depth τ, such that $\exp(-\tau)$ is the resulting transmission – often referred to as the 'flux'. We begin by calculating τ for the IGM in two very different approximations.

2.1 The fluctuating Gunn–Peterson approximation

The Lyman-α optical depth observed at wavelength λ due to a *homogeneous* density distribution of neutral hydrogen with proper number density $n_{\mathrm{H\,I}}(z)$ in a cosmological setting, is given by

$$\tau(\lambda) = \int_0^{z_s} \sigma \left(\frac{(1+z)c}{\lambda} \right) n_{\mathrm{H\,I}}(z) \frac{c\,dz}{(1+z)H(z)}, \tag{1}$$

(Gunn & Peterson 1965), where c is the light speed, σ is the Lyman-α cross-section as function of frequency c/λ, $\lambda_0 \sim 1215.67$ Å is the laboratory wavelength of the H I $n = 1 \rightarrow 2$ transition, and $H(z)$ the

Hubble parameter at redshift z (see e.g. Meiksin 2009 for an extensive recent review of the relevant physics). Since the proper length dr corresponding to a redshift interval dz is $dr = c\,dz/[(1+z)H(z)]$, equation (1) simply states that a column of neutral hydrogen $n_{\mathrm{H\,I}}dr$ contributes $\sigma\,n_{\mathrm{H\,I}}dr$ to the optical depth. Here, z_s is the redshift of the source.

Structure formation results in the growth of the amplitude of fluctuations in the density field. This causes the transmission as a function of wavelength to be in the form of relatively well-defined 'absorbers' (Lynds 1971), collectively referred to as the Lyman-α forest (Weymann et al. 1981). At higher z, the absorbers blend into each other such that regions of near zero transmission are interrupted by small clearings (a Lyman-α jungle), whereas at low z a near unity transmission is occasionally interrupted by a single absorber (a Lyman-α savannah).

When the gas is in photoionization equilibrium, the optical depth resulting from a single absorber depends on density and temperature as $\tau \propto \rho^2\,T^{-0.76}$ where $T^{-0.76}$ is (approximately) the temperature dependence of the hydrogen recombination rate. Taking peculiar velocities and thermal broadening into account as well results in the 'fluctuating Gunn–Peterson' approximation (Croft et al. 1998; Gnedin & Hui 1998) for the optical depth,

$$\tau(v) = \sum \int \frac{n_{\mathrm{H\,I}}}{1+z} \left| \frac{dv'}{dx} \right|^{-1} \sigma_\alpha dv' \tag{2}$$

$$\sigma_\alpha = \sigma_0 \frac{c}{b\sqrt{\pi}} e^{-(v-v_0)^2/b^2} \tag{3}$$

$$\sigma_0 \equiv \left(\frac{\pi e^2}{m_e c} \right) \left(\frac{1}{4\pi\epsilon_0} \right) f_{\mathrm{lu}}, \tag{4}$$

where e is the electric charge of an electron, m_e the electron mass, ϵ_0 is the electric constant, and f_{lu} is the upward oscillator strength (usually referred to as the 'f' factor). The velocity coordinate v is related to the observed frequency through

$$v = \frac{v_0}{1+\bar{z}} \left(1 - \frac{v}{c} \right), \tag{5}$$

where $v_0 = c/\lambda_0$ is the Lyman α frequency in the lab, $\bar{z}$ is a mean redshift of interest. The integral is now over the profile of each individual 'absorber', the Jacobian $|dv'/dx|$ takes into account velocity gradients, and the sum is over many absorbers. The Gaussian profile expresses (thermal) broadening and neglects the intrinsic line profile of the Lyman-α transition.

The temperature of the IGM is set by the balance between photoionization heating of the UV-background, the adiabatic compression, and the adiabatic expansion of the universe. This introduces the temperature–density relation which, for densities around the cosmic mean, is approximately a power law (Hui & Gnedin 1997)

$$T = T_0 \left(\frac{\rho}{\langle \rho \rangle} \right)^{\gamma-1} \equiv T_0\,\Delta^{\gamma-1}, \tag{6}$$

where T_0 is the temperature at the mean density $\langle \rho \rangle$, and Δ the density contrast. Close to reionization the gas is nearly isothermal, $\gamma \sim 1$, whereas asymptotically long after reionization, $\gamma \rightarrow 1 + 1/1.7$ (Hui & Gnedin 1997; Theuns et al. 1998). The $z < 5$ Lyman-α forest can be reasonably well described as being a sum of individual absorbers, and we discuss their properties next.

2.2 Lyman-α absorbers

The simplest single absorber, a cloud of uniform density, temperature T, and with H I column density $N_{\mathrm{H\,I}}$, produces a Gaussian

absorption line when neglecting the intrinsic Lyman-α line profile,

$$\tau(v) = \tau_0 e^{-(v-v_0)^2/b^2},$$
$$\tau_0 = \frac{\sigma_0 c}{\sqrt{\pi}} \frac{N_{\mathrm{H\,I}}}{b}. \tag{7}$$

The line centre is at velocity $v_0 = c\log(1+z) + v_{\mathrm{pec}}$ for an absorber at redshift z, with peculiar velocity v_{pec}. Equation (7) can be obtained from equation (2) in the limit that $n_{\mathrm{H\,I}}|du/dx|^{-1}$ has a peak at u_0 with a width in velocity space much less than the thermal width b, this is the so called narrow-maximum limit in Hui, Gnedin & Zhang (1997).

Several processes contribute to the broadening b of the line. The thermal broadening is given by

$$b_{\mathrm{T}}^2 \equiv \frac{2k_{\mathrm{B}}T}{m_{\mathrm{H}}} \tag{8}$$

$$= \left(12.8\,\mathrm{km\,s^{-1}}\right)^2 \left(\frac{T_0}{10^4\mathrm{K}}\right) \Delta^{\gamma-1}, \tag{9}$$

with m_{H} the mass of the hydrogen atom and k_{B} Boltzmann's constant. The second line applies to gas on a temperature–density relation of the form $T = T_0 \Delta^{\gamma-1}$ from equation (6).

A more realistic absorber should have at least *some* density structure. Assuming the line centre corresponds to a maximum ρ_0 in density, a Taylor-expansion in velocity space yields to lowest order

$$\log(\rho(v)/\rho_0) = -(v-v_0)^2/b_\rho^2. \tag{10}$$

Real Lyman-α absorbers may not be strongly peaked, but note that what matters is not the density profile of the absorber, but its *neutral* density. Since $n_{\mathrm{H\,I}} \propto \rho^2$ for isothermal gas in ionization equilibrium, peaks in neutral gas density are better defined than the maxima in density – as we will show using numerical simulations in the next section.

The absorption profile of this more realistic absorber is then a convolution of the Gaussians of equations (7) and (10), i.e. another Gaussian, with width

$$b^2 = b_{\mathrm{T}}^2 + b_\rho^2. \tag{11}$$

What sets the velocity extent b_ρ? Absorbers at modest density contrast are expanding at a rate somewhat smaller than the Hubble rate, suggesting that $b_\rho \sim \lambda H$, with λ the physical extent of the structure along the line of sight. Based on the papers of Schaye (2001) and Gnedin & Hui (1998), we expect the physical extent of the absorbers to be of the order of the Jeans length λ_{J}, defined in equation (15) below (see also Miralda-Escude & Rees 1993). In the model of Schaye (2001), absorbers are assumed to be locally in near-hydrostatic equilibrium, with column density related to density by

$$N_{\mathrm{H\,I}} \sim n_{\mathrm{H\,I}} \lambda_{\mathrm{J}}, \tag{12}$$

and hence 'size' λ_{J}. Because the dynamical times of low-density absorbers are long, the structures are still expanding, and are not exactly in hydrostatic equilibrium but are lagging behind. This is encapsulated by the 'filtering scale' $\lambda_{\mathrm{F}} = 2\pi/k_{\mathrm{F}}$ of Gnedin & Hui (1998) which depends on the full history of the Jeans length over cosmic time and hence depends on the thermal history, not just the instantaneous Jeans length. The physical 'extent' of the absorber in this approximation is then $\sim 1/k_{\mathrm{F}}$, therefore its velocity extent is $\sim H(z)/(k_{\mathrm{F}}(1+z)) \approx \lambda_{\mathrm{J}} H(z)/(2\pi)$, where λ_{J} is now the physical –

as opposed to comoving – extent of the absorber. This then motivates us to write

$$b_\rho = f_{\mathrm{J}} \frac{\lambda_{\mathrm{J}} H(z)}{2\pi}. \tag{13}$$

The factor f_{J} parameterizes the time-dependent Jeans smoothing of the gas density profiles, and we expect it to be of order unity.

For gas on a power-law temperature–density, the values of the sound speed and Jeans length depend on the density contrast Δ as

$$c_{\mathrm{s}}^2 = \left(\frac{5k_{\mathrm{B}}T}{3\mu m_{\mathrm{H}}}\right)$$

$$= (15.2\,\mathrm{km\,s^{-1}})^2 \left(\frac{T_0}{10^4\mathrm{K}}\right) \Delta^{\gamma-1} \tag{14}$$

$$\lambda_{\mathrm{J}}^2 \equiv \frac{c_{\mathrm{s}}^2 \pi}{G\rho_{\mathrm{t}}}$$

$$= \frac{(5/3)\pi k_{\mathrm{B}} T_0}{\mu m_{\mathrm{H}} G\rho_{\mathrm{t}}(z=0)(1+z)^3} \Delta^{\gamma-2}$$

$$\approx (260\,\mathrm{kpc})^2 \left(\frac{T_0}{10^4\mathrm{K}}\right) \Delta^{\gamma-2}$$

$$\times \left(\frac{\Omega_{\mathrm{m}}}{0.307}\right)^{-1} \left(\frac{h}{0.6777}\right)^{-2} \left(\frac{1+z}{4}\right)^{-3}, \tag{15}$$

where μ is the mean molecular weight and $\rho_{\mathrm{t}} = \rho_{\mathrm{dm}} + \rho_{\mathrm{b}}$ is the *total* density, dark matter plus baryons, G is the gravitational constant, Ω_{m} is the matter density. We write the Hubble parameter at redshift z as $H(z)$, with $H_0 = 100h\,\mathrm{km\,s^{-1}\,Mpc^{-1}}$ its value today. The numerical values assume $\mu = 0.59$, that dark matter and gas move together, and for reference we use the Planck Collaboration (2013) values for the cosmological parameters. Numerically, the broadening due to Jeans smoothing is thus of order

$$b_\rho^2 = f_{\mathrm{J}}^2 \frac{10\,k_{\mathrm{B}}T}{9\mu\,m_{\mathrm{H}}\Delta} \frac{H^2(z)}{H_0^2\,\Omega_{\mathrm{m}}(1+z)^3}$$

$$\approx (11.1\,\mathrm{km\,s^{-1}})^2 \left(\frac{f_{\mathrm{J}}}{0.88}\right)^2 \left(\frac{T_0}{10^4\mathrm{K}}\right) \Delta^{\gamma-2}, \tag{16}$$

independent of redshift in the high-redshift approximation $H(z) \propto (1+z)^{3/2}$. The model of Hui & Rutledge (1999) uses a very similar reasoning to infer line widths; b_ρ is usually referred to as the 'Hubble broadening'. We demonstrate below that a value of $f_{\mathrm{J}} \sim 0.88$ describes our numerical simulations well at $z=3$.

The total broadening, b, of the absorber is then

$$b^2 = b_{\mathrm{T}}^2 \left[1 + f_{\mathrm{J}}^2 \frac{5}{9\mu} \Delta^{-1}\right]$$

$$\approx b_{\mathrm{T}}^2 \left[1 + 0.75 \left(\frac{f_{\mathrm{J}}}{0.88}\right)^2 \Delta^{-1}\right]. \tag{17}$$

The line widths of weak absorbers ($\Delta \lesssim 1$) are increasingly dominated by Hubble broadening, $b^2 \sim b_{\mathrm{T}}^2 \Delta^{-1} \propto \Delta^{\gamma-2}$, and hence the filtering scales determines their widths. Hubble expansion plays a smaller role for stronger lines, with line widths ultimately set by thermal broadening alone. Equation (17) smoothly interpolates between filtering and pure thermal broadening. However, we note that for typical $z \sim 3$ absorbers with $\Delta \sim 3$, Hubble broadening still plays a significant role, increasing b by almost 70 per cent compared to thermal broadening alone. It might be possible to measure the extent of absorbers in real space using close quasar pairs (see Rorai,

Hennawi & White 2013; the impact of Jeans length on quasar pairs was also considered in Peeples et al. 2010). The extra broadening discussed here is a longitudinal measure of the Jeans length, as opposed to the transverse Jeans length probed with pairs.

The Gaussian shape of the absorber directly relates column density and width,

$$b^2 = -\frac{2\tau^2}{\tau\,\tau'' - \tau'^2} = -\frac{2\tau_0}{\tau_0''} \tag{18}$$

$$N_{\mathrm{H\,I}} = \frac{\sqrt{\pi}}{\sigma_0 c} b\tau_0\,, \tag{19}$$

where $\tau' \equiv d\tau/dv$, $\tau'' \equiv d^2\tau/dv^2$, and the subscript 0 indicates that the quantity is to be evaluated at the (local) maximum of the optical depth. We will use these relations below. Equations (18)–(19) follow directly from equations (7).

3 BROADENING OF LYMAN-α ABSORBERS IN SIMULATIONS

3.1 Mock spectra from simulations

We use the REFERENCE model of the OWLS suite (Schaye et al. 2010) to test our model for line broadening. Briefly, the OWLS suite is a set of cosmological hydrodynamical simulations performed with the GADGET-3 code, an improved version of GADGET-2 last described by Springel (2005), with subgrid models for unresolved galaxy formation physics, in particular star formation, and feedback by and enrichment from stars, as described in Schaye & Dalla Vecchia (2008), Dalla Vecchia & Schaye (2008) and Wiersma et al. (2009b), respectively. Although efficient feedback from star formation results in outflows from galaxies in this simulation, such winds do not have a significant impact on the Lyman-α forest for reasons discussed in Theuns et al. (2002c), see also Viel et al. (2013). Most relevant for this paper is that we simulate a Λ CDM model using 512^3 smoothed particle hydrodynamics particles that represent the gas, and an equal number of dark matter particles. The computational volume is a periodic box of comoving size $25\,h^{-1}$ Mpc on a side. The masses of the gas particles ($\sim 2 \times 10^6\,h^{-1}\,\mathrm{M}_\odot$) are sufficiently low to obtain numerical convergence for the line widths (Theuns et al. 1998). Photoheating of the gas in the presence of an optically thin UV/X-ray background from Haardt & Madau (2001) is implemented using interpolation tables from Wiersma, Schaye & Smith (2009a).

Photoheating, adiabatic processes, shocks from structure formation and feedback from galactic winds and radiative cooling produce the temperature–density relation shown in Fig. 1(a) at redshift $z = 3$. Most of the gas is on a tight temperature–density relation, $T = T_0 \Delta^{\gamma - 1}$, with $T_0 \approx 15\,000$ K and $\gamma \approx 1.32$ for $\Delta \lesssim 5$, and this gas is the main reservoir responsible for producing the Lyman-α forest. There is gas at significantly higher temperatures at these densities, which results from structure formation and feedback. The increased importance of radiative cooling decreases the amount of hot gas at higher densities, and an equilibrium sequence where radiative cooling and photoheating balance results in the appearance of significant amounts of gas at $T \sim 10^4$ K. This higher density gas results in Lyman-limit and damped Lyman-α absorbers (e.g. Altay et al. 2011). Self-shielding is important for this higher density gas, and the impact of feedback becomes more important (Altay et al. 2013).

Given a snapshot of the simulation at some redshift (we use $z = 3$ in this paper), we generate mock Lyman-α spectra using the method described in Theuns et al. (1998) but using the interpolation tables of
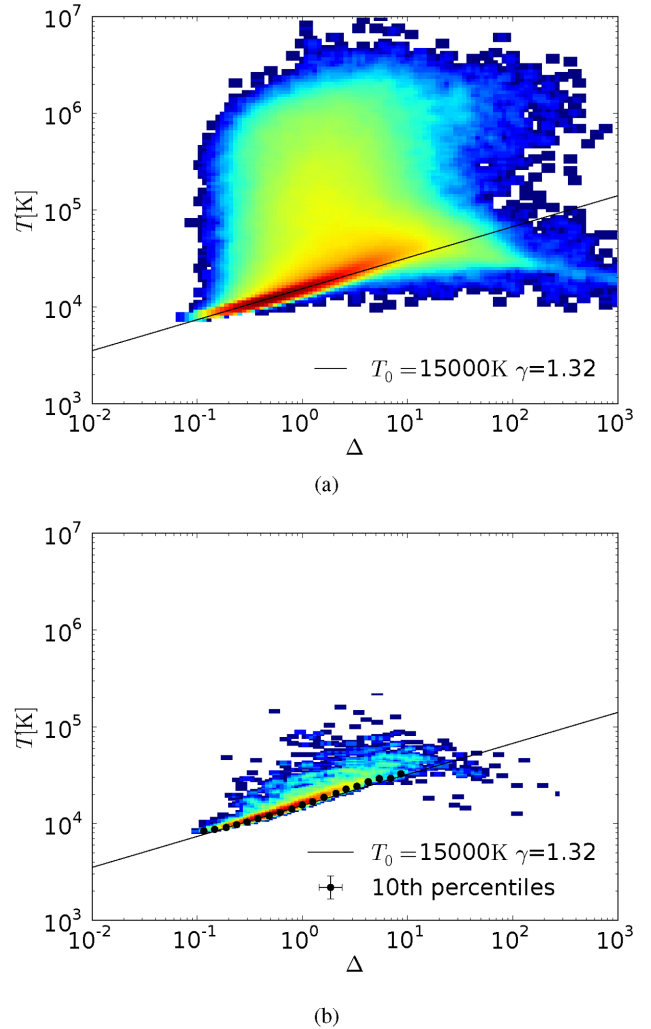

Figure 1. Mass-weighted (top panel) and optical depth weighted (bottom panel) temperature–density relation in the REFERENCE OWLS run at $z = 3$. Values in the bottom panel are evaluated at the locations of maxima in the optical depth. Colours are a measure of the density of points in these plots, and $\Delta = \rho/\langle\rho\rangle$. In the lower panel, the black dots indicate the median temperature in bins of Δ with error bars computed by bootstrap resampling. The black solid line in both panels show the power-law $T = T_0\Delta^{\gamma - 1}$ that best fits the black dots for $\Delta < 3$. There is a much larger scatter in T versus Δ in the top panel than in the bottom panel, but this shocked gas contributes little to the Lyman-α forest. The lower envelope of points in the T–Δ relation in the bottom panel mirrors the temperature–density relation of the lower envelope in the top panel, demonstrating that the optical depth weighted temperature at the optical depth maxima of absorption lines follows very closely the T–Δ relation of the photoheated IGM.

Wiersma et al. (2009a) to relate total to neutral hydrogen density. We generate these spectra at very high resolution using pixels of width $\sim 2\,\mathrm{km\,s}^{-1}$, much narrower than any of the absorption features that appear. Importantly, we neither add noise nor instrumental broadening to mimic observed spectra – limiting our analysis to comparing our model to idealized observations. Each sight-line is parallel to a coordinate axis of the simulation volume, and we use velocity pixels of size $v = H(z)L/[(1 + z)N]$, where $L = 25\,h^{-1}$ Mpc is the comoving box size, and N the number of pixels. We calculate $\tau(v)$, $T(v)$ and $\rho(v)$, where T and ρ are the *optical depth weighted* temperature and density, respectively (see Schaye et al. 1999).
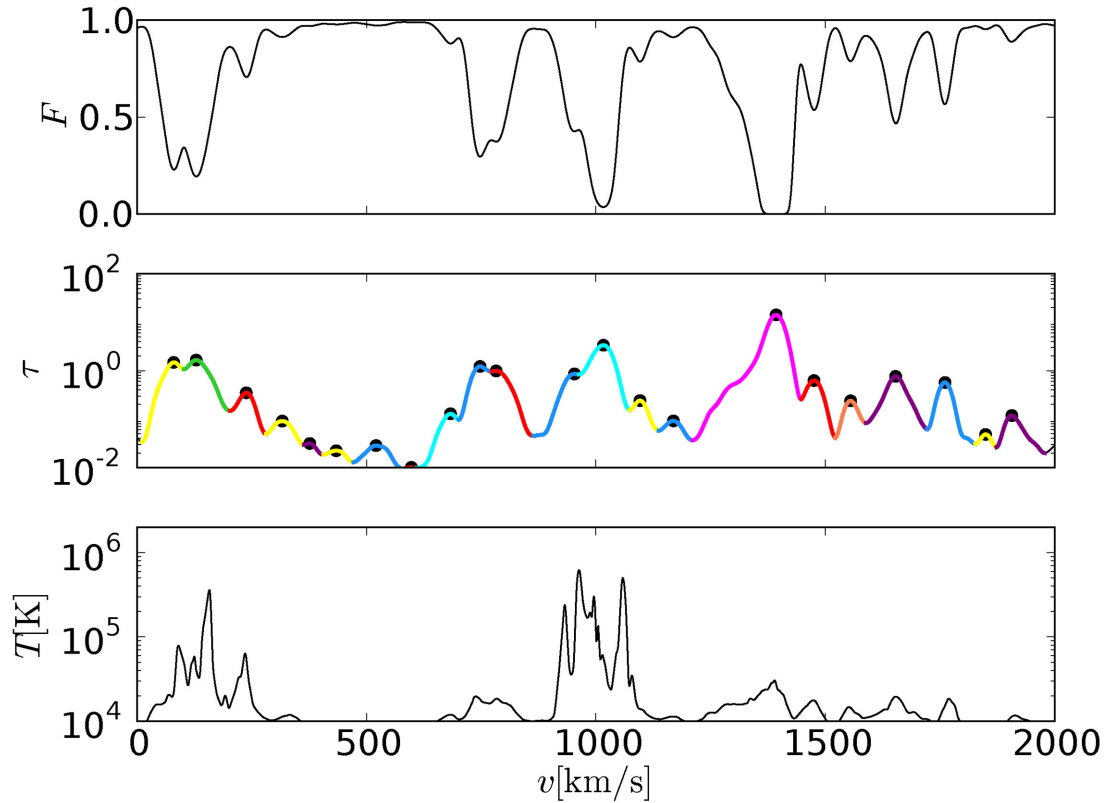
Figure 2. A stretch of a simulated spectrum at redshift $z \sim 3$. From top to bottom, we show the transmission $F \equiv (-\tau)$, optical depth τ, and optical depth weighted temperature, T, as function of velocity v. Individual lines are regions of the spectra between two minima in optical depth, they are coloured using different colours, with a filled circle at the maximum τ for each line. Note that T is not constant over a line.

Unless explicitly stated, we will always use optical depth weighted quantities for variables measured from spectra.

In Fig. 1(b), we plot values of optical depth weighted temperature versus density, for pixels that correspond to local maxima in the optical depth from these mock spectra. Most points lie close to the lower envelope of the points in the scatter plot, which tracks the same T–Δ relation as the lower envelope in Fig. 1(a). The scatter around this relation is much less in Fig. 1(b), because the shocked gas that causes the scatter to higher T in Fig. 1(a) contributes little to the optical depth. At higher $\Delta \gtrsim 10$, T decreases with increasing Δ, reflecting the effects of radiative cooling also apparent in Fig. 1(a).

3.2 Identifying individual absorbers

We identify individual absorbers (or 'lines') with regions of the spectrum between two minima in the optical depth, dissecting the whole spectrum in a set of unique stretches. An example spectrum is shown in Fig. 2, with different lines coloured differently, and with diamonds at the locations of local maxima in τ. Unsurprisingly, the temperature varies across a line, and hence assigning a single temperature (or density) to a line is necessarily somewhat ambiguous. We could decide to associate to a line the maximum, the (weighted) mean or the value corresponding to the maximum of the line for any given physical quantity. In the following, where not specified otherwise, we will associate to the line the value of the physical quantity that corresponds to the optical depth weighted value evaluated at the local maximum in optical depth. This method for identifying lines is not directly applicable to observed spectra in the presence of noise. Such spectra should be smoothed to avoid incorrectly identifying

noise features with small lines, however this may lead to missing true weak absorbers. Preliminary analysis shows that fitting a Gaussian over a set of contiguous pixels to calculate the derivatives that appear in equation (18) is promising, we will report on this in a future paper.

As demonstrated in Fig. 1, the (real-space) temperature–density relation of the IGM in the simulation translates approximately to a power-law (optical depth weighted) temperature–density relation for the lines generated in mock spectra. Most lines follow $T = T_0 \propto \Delta^{\gamma-1}$ up to $\Delta \lesssim 3$, with some scatter to significantly higher T, but none scatter significantly *below* this line. However for $\Delta \gtrsim 3$, the median temperature does fall below the power-law fit: this is because this gas cools radiatively, and this results in a decrease in T with higher Δ for the real-space temperature–density relation as well. Note further that the T–Δ relation is only approximately a power law, with evidence for some curvature even over a relatively narrow Δ range. Finally, note that in the absence of noise, we see that the majority of lines have $0.1 \lesssim \Delta \lesssim 10$.

The optical depth profile of several of the lines in Fig. 2 appear reasonably Gaussian in shape near their maxima, and we will investigate to what extent their widths follow equation (17). However, it is also clear that some lines blend with nearby lines, and we will show below that this 'clustering' impacts how well we can infer the underlying T–Δ relation from spectra – even in the absence of noise.

We suggested that line broadening has a contribution b_ρ due to the spatial extent of the absorber as described by equation (13). To test this directly, we should plot b_ρ versus Δ. However, maxima in τ do not correspond directly to maxima in Δ because of
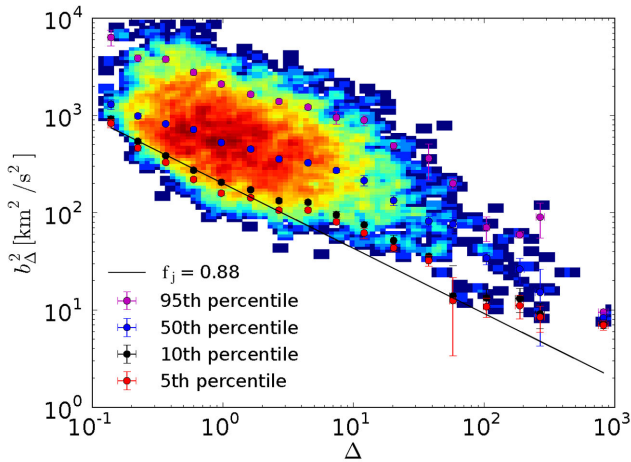
Figure 3. Velocity extent of absorbers in real-space b_Δ versus density contrast Δ for lines identified in mock spectra without peculiar velocities. Colours indicate density of points in the plot. The 5th, 10th, 90th and 95th percentiles of b_Δ in bins of Δ are shown as symbols with bootstrap errors. Line widths decrease with increasing density, opposite to the case of thermal broadening. This behaviour is captured by the solid black line, the broadening b_ρ from equation (13) for $f_J = 0.88$, which fits the lower percentiles of the $b_\Delta - \Delta$ relation well in shape and amplitude for $\Delta \lesssim 3$.

Figure 4. Total broadening $b^2 \equiv -2\tau/\tau''$ of absorbers at line centres as a function of density contrast Δ for lines identified in mock spectra. Colours indicate density of points in the plot. Black dots with bootstrap error bars denote the location of the 10th lower percentile of b in bins of Δ. The dotted red line is the thermal width from equation (9) for the temperature–density relation from Fig. 1(a); lines are invariably wider than b_T except at $\Delta \gtrsim 10$. The solid black line is the model of equation (11) with $f_J = 0.88$, for the same T–Δ power-law relation. It describes the black dots very well up to $\Delta \sim 3$, above which the simulation's T–Δ relation is not well fitted by a power law. The dashed magenta line is again the model of equation (11) but now using the measured T–Δ relation rather than a power-law fit: it captures the down-turn in b for $\Delta \gtrsim 3$ due to the onset of radiative cooling.

peculiar velocities. Therefore, to unambiguously identify a line with a density structure, we generate mock spectra setting peculiar velocities to zero. We later show that this has very little effect on the line broadening (see also Fig. 5). For each line identified in these mock spectra, we can now unambiguously identify the corresponding density stretch that gives rise to that line. However, the shape of the density structure of lines is often complex and it is not immediately apparent what extent to associate with a given line. We decided to use the following prescription. For each line, we determine its start and end velocity, v_1 and v_2, the location (v_{max}) and height (Δ_{max}) of the maximum density, and the integral $I \equiv \int_{v_1}^{v_2} \Delta(v) \, dv$. We now determine the value of b_Δ of the Gaussian profile, $G(\Delta) = \Delta_{max} \exp(-(v - v_{max})^2/b_\Delta^2)$, for which $\int_{v_1}^{v_2} G(v) \, dv = I$. In other words, we define the extent of the absorber, b_Δ, as the width of the Gaussian that has the same integral and maximum value as the line itself. If the line *were* a Gaussian, then b_Δ would simply be its width. Further details on the fitting procedure can be found in Appendix B. We expect that $b_\Delta \sim b_\rho$ from equation (13).

In Fig. 3, we plot b_Δ^2 versus Δ for all lines identified in mock spectra generated while ignoring peculiar velocities. As before, colour encodes the number density of lines in this plot, and 5th, 10th, 50th and 95th percentiles are plotted as symbols with bootstrap error bars. Values of b_Δ^2 *increase* with decreasing Δ – the opposite of what is expected from thermal broadening. The solid line indicates b_ρ^2 from equation (13) with $f_J = 0.88$ applied to gas with the T–Δ relation $T = 15\,000\,\mathrm{K}\,\Delta^{1.3-1}$ which, as we showed earlier, fits the actual temperature–density relation of the simulation well for $0.1 \lesssim \Delta \lesssim 3$. Fig. 3 shows that both the 5th and 10th percentiles follow the solid line well over the same Δ range. This implies that b_ρ, with $f_J = 0.88$, is indeed a good estimate of the width of the absorbers in real space.

Given that our estimate of the broadening of the density profile works well, we plot the total line broadening (including peculiar velocities) versus density contrast, and compare it to the model of equation (17) (Fig. 4). As before, the colour represents the density
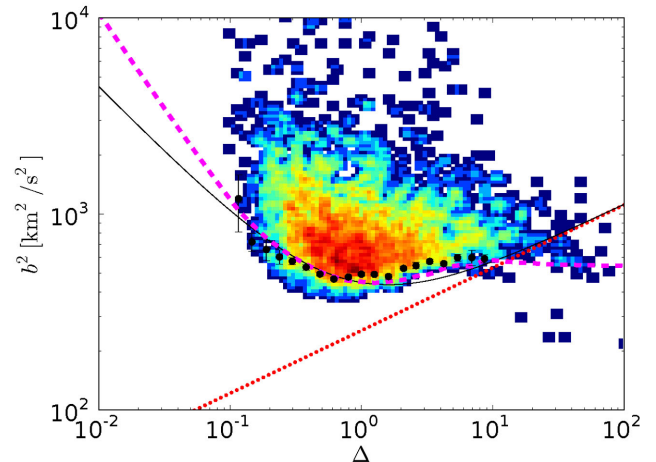
of points in the plot. We compute b from the curvature of the optical depth profile $\tau(v)$ using equation (18); fitting a Gaussian to the pixels close to the maximum yields very similar values of b. Values of b–Δ for individual lines show a larger scatter in b at given Δ, but there is a well-defined lower envelope below which few lines appear. This lower envelope is traced by the 10th percentile of b values in narrow bins of Δ, plotted using black symbols with bootstrap errors. The red dashed line indicates the thermal broadening, b_T, from equation (9), using the power-law fit to the temperature–density relation measured in the simulation. For $\Delta \lesssim 10$, the measured broadening along the cut-off is significantly wider than b_T, with the discrepancy between the two increasing with decreasing Δ. The solid black line shows $b_T^2 + b_\rho^2$ as a function of Δ from equation (17), again using the best-fitting power-law temperature–density relation, and adopting the value $f_J = 0.88$ found above. It captures accurately the dependence of the broadening on Δ for the lower envelope of the absorption lines traced by the 10th percentile for $\Delta \lesssim 3$, in particular reproducing the measured *upturn* in b^2 for $\Delta \lesssim 1$. Because the solid black line assumes that the relation between temperature and density is a power law, it does not describe the simulated b–Δ relation well above $\Delta \sim 3$. The dashed black line uses the median value of the temperature at a given density for absorption lines when calculating the Jeans smoothing term b_ρ in equation (13), rather than a power law. It does much better in capturing the downturn in b–Δ at $\Delta \gtrsim 10$. We conclude from this plot that the model in which the line broadening is a combination of thermal and Jeans smoothing, equation (17) describes the lower envelope in the b–Δ plane well. Note that deviations of the true temperature–density relation from a power law, and Jeans smoothing, cause the T–Δ relation to be non-monotonic, with a minimum value of b for $\Delta \sim 1$ in this particular simulation at this particular redshift.
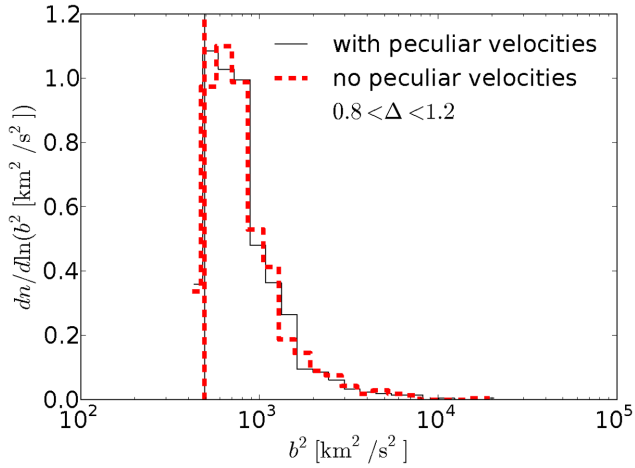
Figure 5. Histogram of line broadening $b^2 = -2\tau/\tau''$ for simulations with and without peculiar velocities, shown as solid black and dashed red lines, respectively. The 10th percentiles of narrowest lines are indicated by vertical lines. The impact of peculiar velocities on the distribution of b values is small.

Peculiar velocities are not the cause of the appearance of lines that are much *wider* than the broadening b computed from equation (17). We compare the distribution of b values for lines identified in mock spectra with and without peculiar velocities in Fig. 5. The peculiar velocities do not have a large effect on the broadening, if anything they make lines slightly *narrower*, see also Theuns, Schaye & Haehnelt (2000).

Our analytic expression for broadening, equation (17), provides only a lower limit on the width of a collection of lines in the Lyman α forest. The additional broadening can be partially attributed to the underlying density structure in the absorber (Hui & Rutledge 1999), for example in terms of the angle under which the sight-line intersects the filament that corresponds to the absorber. However, another important contribution that is not easily captured by linear theory is the *clustering* of density peaks. We illustrate this in Fig. 6, comparing a mock spectrum with the original T–Δ relation with the same spectrum now computed assuming $T = 100$ K everywhere. We see that some individual absorption lines identified in the solid red spectrum have several underlying density maxima. If the temperature of the gas is low, as in the case of the black dotted spectrum, then these individual density maxima give rise to their own absorption lines. But if the gas is sufficiently hot, then thermal and Hubble broadening can merge multiple individual components into one much wider line. The width of that absorber is not described well by our model. We conclude that it is the clustering of density maxima that gives rise to the lines that are much wider than expression b from equation (17). Another way to demonstrate this is to count the number of individual density peaks for each absorber: we find that absorbers with widths close to that from equation (17) typically have only one density maximum, whereas those that are significantly wider correspond to several underlying peaks.
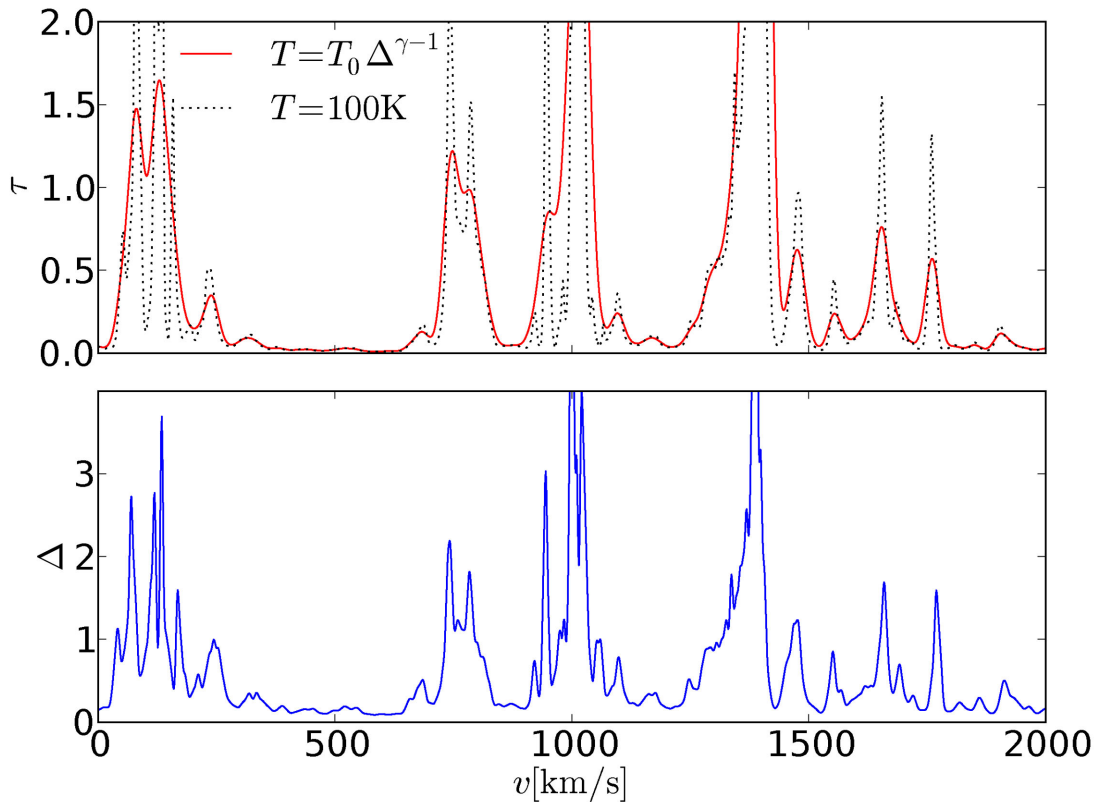

Figure 6. Optical depth τ (top panel) and corresponding density contrast Δ (bottom panel) for mock spectra for the simulation with the original temperature–density relation (solid red line) and for the case where $T = 100$ K everywhere (dotted black line). Clustering of density peaks in real space makes some of the absorption lines much wider than the estimate of b from equation (17), for example the wider lines around $v \sim 800\,\mathrm{km\,s^{-1}}$ and $v \sim 1000\,\mathrm{km\,s^{-1}}$. Thermal broadening and Hubble broadening together smooth the individual peaks seen in the underlying density field into one wide line, whose width cannot be described accurately by equation 17.

4 INFERRING THE TEMPERATURE–DENSITY RELATION FROM OBSERVABLES

Our description of line broadening so far used b and Δ to relate temperature to density, yet density contrast Δ is not directly measurable. Here, we investigate whether we can use the column density $N_{\mathrm{H\,I}}$ of the line instead. Following the reasoning of Schaye (2001), we make the *Ansatz* that the column density, density, and extent of the line are related by

$$N_{\mathrm{H\,I}} \sim n_{\mathrm{H\,I}} f_{\mathrm{J}} \lambda_{\mathrm{J}} . \tag{20}$$

For highly ionized gas in photoionization equilibrium

$$\frac{n_{\mathrm{H\,I}}}{n_{\mathrm{H}}} = \alpha_{\mathrm{H\,II}} n_{\mathrm{e}} \Gamma^{-1}$$

$$\approx 5.6 \times 10^{-6} \left(\frac{n_{\mathrm{H}}}{1.2 \cdot 10^{-5} \mathrm{cm}^{-3}} \right)$$

$$\times \left(\frac{T}{10^4 \mathrm{K}} \right)^{-0.76} \left(\frac{\Gamma}{10^{-12} \mathrm{s}} \right)^{-1} , \tag{21}$$

where

$$\alpha_{\mathrm{H\,II}} = \alpha_0 \left(\frac{T}{10^4 \mathrm{K}} \right)^{-0.76}$$

$$\alpha_0 = 4 \times 10^{-13} \mathrm{cm}^3 \mathrm{s}^{-1} , \tag{22}$$

is the value of the case-A recombination coefficient as a function of temperature, n_{e} is the electron number density, n_{H} is the total hydrogen number density, and Γ the photoionization rate. Combining these with the expression of the Jeans length from equation (15) yields

$$N_{\mathrm{H\,I}} = \frac{3\sqrt{10}}{64\pi} f_{\mathrm{N}} f_{\mathrm{J}} (2 - Y)(1 - Y) \frac{\Omega_{\mathrm{b}}^2}{\Omega_{\mathrm{m}}^{1/2}} \frac{\alpha_0}{\Gamma} \frac{H_0^3}{(G m_{\mathrm{H}})^2}$$

$$\times \left(\frac{k_{\mathrm{B}} 10^4 \mathrm{K}}{\mu m_{\mathrm{H}}} \right)^{1/2} \left(\frac{T}{10^4 \mathrm{K}} \right)^{-0.26} (1 + z)^{9/2} \Delta^{3/2}$$

$$\equiv N_0 \frac{f_{\mathrm{N}}}{0.3} \frac{f_{\mathrm{J}}}{0.88} \left(\frac{T}{10^4 \mathrm{K}} \right)^{-0.26} \Delta^{3/2} , \tag{23}$$

where numerically

$$N_0 = 1.4 \times 10^{13} \mathrm{cm}^{-2} \left(\frac{\Gamma}{10^{-12} \mathrm{s}^{-1}} \right) \left(\frac{1 + z}{4} \right)^{9/2}$$

$$\times \left(\frac{\Omega_{\mathrm{b}}}{0.04825} \right)^2 \left(\frac{\Omega_{\mathrm{m}}}{0.307} \right)^{-1/2} \left(\frac{h}{0.6777} \right)^3 . \tag{24}$$

Here, f_{N} is the proportionality factor implicit in equation (20) which we show below is ~ 0.3, and the numerical value for N_0 is for very highly ionized ($\mu = 0.59$) primordial gas with the Planck Collaboration (2013) cosmological parameters, and Y is the primordial helium abundance. For a power-law temperature–density relation, $T = T_0 \Delta^{\gamma-1}$, the hydrogen column density depends only weakly on temperature, $N_{\mathrm{H\,I}} \propto T_0^{-0.26}$, and it scales with density contrast as $\Delta^{1.76-0.26\gamma}$. We compare the results from equation (23) to our simulation in Fig. 7, where we find the best fit of the model to the 10th percentile distribution of the $N_{\mathrm{H\,I}}$ versus Δ, the justification of this choice is in Appendix A. The model fits very accurately the results from the simulation over nearly four order of magnitude in column density, as also shown in Rahmati et al. (2013) and Tepper-García et al. (2012).

Finally, we combine equation (23) with equation (17) to obtain a relation between the two observables quantities, namely the column
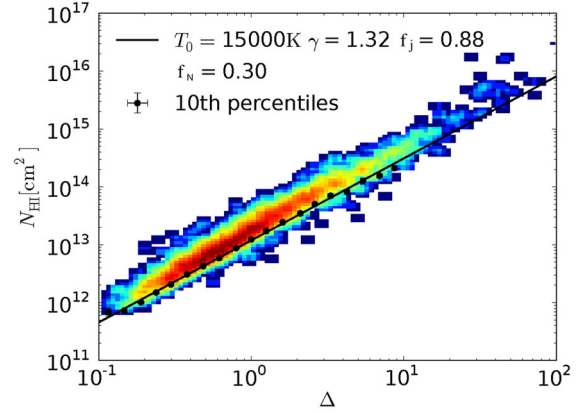

Figure 7. The neutral hydrogen column density of absorption lines versus density contrast for the REFERENCE model at $z = 3$; colours are a measure of the density of points in the plot. Black dots denote the 10th percentiles of column density in logarithmic bins of Δ. The solid black line corresponds to the model of equation (19), using the value of Γ appropriate for the REFERENCE model with values of T_0, γ and f_{J} taken from Fig. 4, and for $f_{\mathrm{N}} = 0.3$. This value of f_{N} is the result of best-fitting equation (19) to the 10th percentiles, for $\Delta \leq 0.3$. This provides an excellent fit to the results from the simulation over 4 orders of magnitude in column density.

density $N_{\mathrm{H\,I}}$ and the lower envelope of line widths at a given column density, b, in terms of underlying temperature–density relation of the gas, as

$$b_{\mathrm{T}}^2 = \frac{2k_{\mathrm{B}} T_0}{m} N^{(\gamma-1)/(1.76-0.26\gamma)}$$

$$b^2 = b_{\mathrm{T}}^2 \left[1 + 0.75 \left(\frac{f_{\mathrm{J}}}{0.88} \right) N^{-1/(1.76-0.26\gamma)} \right]$$

$$N \equiv \left(\frac{N_{\mathrm{H\,I}}}{N_0} \right) \left(\frac{T_0}{10^4 \mathrm{K}} \right)^{0.26} \left(\frac{f_{\mathrm{N}}}{0.3} \right)^{-1} \left(\frac{f_{\mathrm{J}}}{0.88} \right)^{-1} . \tag{25}$$

This relation is compared to the $b-N_{\mathrm{H\,I}}$ distribution of the simulation in Fig. 8. Our model for line broadening does well in predicting the minimum line width as a function of column density, in particular predicting correctly that line width is not a monotonic function of column density. At low Δ, line widths increase as Jeans smoothing becomes more important, whereas at high Δ, line widths decrease due to radiative cooling. The underlying $T-\Delta$ relation of the simulation is only approximately a power law; using the relation from the simulation directly in equation (23) improves the agreement between model and simulation further, in particular it might be possible to measure the temperature of denser gas, $\Delta \sim 10$. We illustrate the sensitivity of the $b-N_{\mathrm{H\,I}}$ relation to small changes in T_0 and γ, as well as the fitting parameters f_{J} and f_{N}, in Appendix .

Our model overestimates line broadening of very weak lines, $N_{\mathrm{H\,I}} \lesssim 10^{12.5}$ cm^{-2}, yet it correctly predicts line widths at low-density contrast (see Fig. 4). In Appendix , we show that this is because line width biases how well a line of given column can be associated with a given density contrast. In practise, these lines are too weak to be detected in observed spectra.

5 CONCLUSIONS

We have presented an analytic description of the broadening of lines in the Lyman-α forest, in terms of the temperature, Jeans smoothing and density of the absorbers. Identifying individual absorbers in a spectrum as spectral stretches between two minima in the optical
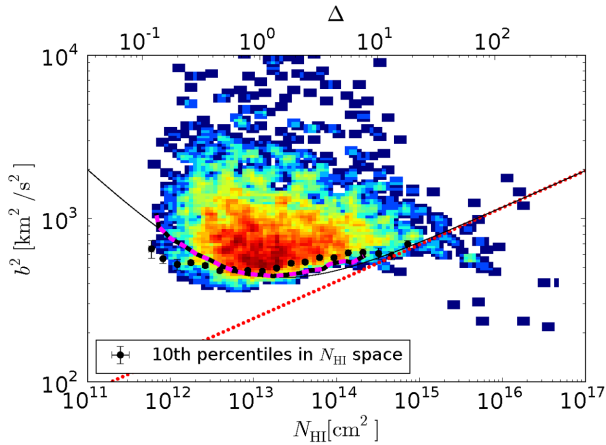
Figure 8. The line-width column density $b^2 - N_{H_I}$ relation in the REFERENCE OWLS model at redshift $z = 3$, with broadening determined from equation (18) and column density from equation (19). The top axis gives the value of the density contrast that corresponds to N_{H_I} from equation (23). Colours denote the density of points in this plot, black dots denote the 10th percentile of b^2 in bins of column density with bootstrap error bars. The dotted red line is the thermal broadening b_T^2 from equation (9) using equation (23) to relate column density to density contrast. The solid black line is our model for broadening of equation (25) using the values T_0 and γ from Fig. 1(a), $f_J = 0.88$ from Fig. 3 and $f_N = 0.3$ from Fig. 7. The black line connecting magenta dashes is equation (25) using the $T-\Delta$ relation measured from the simulation, rather than a power-law fit. The analytic formula describes the minimum line width at a given column density accurately, and works even better if the actual $T-\Delta$ relation is used rather than a power-law fit.

depth, we calculated the line width, b, from the second derivative of the optical depth at the local maximum in τ, $b^2 \equiv -2\tau/\tau''$ (equation 18). We argued that the thermal width of a line, b_T, combined with its width due to Jeans smoothing, b_ρ, sets a lower limit on the total line width, $b^2 \gtrsim b_T^2 + b_\rho^2$. We derived an expression for b_ρ that depends on the temperature T and the density contrast Δ of the absorber, which smoothly interpolates between the filtering length interpretation of line widths from Hui & Gnedin (1997) at low Δ, and the near-hydrostatic equilibrium model of Schaye (2001) at higher Δ. This model gives a good description of the lower values of b at given Δ (Fig. 4). We also discussed the origin of the lines that are significantly wider than the lower envelope, arguing that they result from the clustering of several individual density maxima that cannot be distinguished in the spectrum due to thermal broadening and Jeans smoothing. Such clustering is not captured by our quasi-linear model.

Based on the model of Schaye (2001), we write an expression relating column density to density contrast. Combining this with our model for line broadening yields an analytic expression for the lower envelope of b as a function of column density, N_{H_I} (equation 25). This model describes the lower envelope much better than one based on thermal broadening alone (Fig. 8).

In our interpretation of b, line widths of weaker lines are dominated by the filtering length, which in principle depends on the *thermal history* of the IGM and not just on its instantaneous state. If this is true, then not taking this into account may affect the interpretation of the $b-N_{H_I}$ cut-off in terms of the underlying temperature–density relation of the gas.

Our analytic description of the line broadening opens the way to a new method for determining the IGM thermal state, and in particular for measuring the 'longitudinal' size of the absorbers (the 'filtering length'), that is complementary to what can be measured from close

QSO pairs. This is particularly interesting, because for the first time we have a method to estimate the sizes of the clouds from a single line of sight.

REFERENCES

Abel T., Haehnelt M. G., 1999, ApJ, 520, L13
Aguirre A., Schaye J., 2005, in Williams P., Shu C.-G., Menard B., eds, IAU Colloq. 199: Probing Galaxies through Quasar Absorption Lines. Cambridge Univ. Press, Cambridge, p. 289
Altay G., Theuns T., Schaye J., Crighton N. H. M., Dalla Vecchia C., 2011, ApJ, 737, L37
Altay G., Theuns T., Schaye J., Booth C. M., Dalla Vecchia C., 2013, MNRAS, 436, 2689
Becker G. D., Bolton J. S., Haehnelt M. G., Sargent W. L. W., 2011, MNRAS, 410, 1096
Benson A. J., Lacey C. G., Baugh C. M., Cole S., Frenk C. S., 2002, MNRAS, 333, 156
Bi H., Davidsen A. F., 1997, ApJ, 479, 523
Bolton J. S., Haehnelt M. G., Viel M., Springel V., 2005, MNRAS, 357, 1178
Bolton J. S., Viel M., Kim T.-S., Haehnelt M. G., Carswell R. F., 2008, MNRAS, 386, 1131
Boyarsky A., Lesgourgues J., Ruchayskiy O., Viel M., 2009, J. Cosmol. Astropart. Phys., 5, 12
Bryan G. L., Machacek M. E., 2000, ApJ, 534, 57
Calura F., Tescari E., D'Odorico V., Viel M., Cristiani S., Kim T.-S., Bolton J. S., 2012, MNRAS, 422, 3019
Cen R., Miralda-Escudé J., Ostriker J. P., Rauch M., 1994, ApJ, 437, L9
Compostella M., Cantalupo S., Porciani C., 2013, MNRAS
Cowie L. L., Songaila A., Kim T.-S., Hu E. M., 1995, AJ, 109, 1522
Croft R. A. C., Weinberg D. H., Katz N., Hernquist L., 1998, ApJ, 495, 44
Dalla Vecchia C., Schaye J., 2008, MNRAS, 387, 1431
Davidsen A. F., Kriss G. A., Zheng W., 1996, Nature, 380, 47
Efstathiou G., 1992, MNRAS, 256, 43P

Fukugita M., Hogan C. J., Peebles P. J. E., 1998, ApJ, 503, 518
Garzilli A., Bolton J. S., Kim T.-S., Leach S., Viel M., 2012, MNRAS, 424, 1723
Gnedin N. Y., Hui L., 1998, MNRAS, 296, 44
Gunn J. E., Peterson B. A., 1965, ApJ, 142, 1633
Haardt F., Madau P., 1996, ApJ, 461, 20
Haardt F., Madau P., 2001, in Neumann D. M., Tran J. T. V., eds, Clusters of Galaxies and the High Redshift Universe Observed in X-rays, preprint (ArXiv:astro-ph/0106018)
Hui L., Gnedin N. Y., 1997, MNRAS, 292, 27
Hui L., Rutledge R. E., 1999, ApJ, 517, 541
Hui L., Gnedin N. Y., Zhang Y., 1997, ApJ, 486, 599
Jakobsen P., Boksenberg A., Deharveng J. M., Greenfield P., Jedrzejewski R., Paresce F., 1994, Nature, 370, 35
Lidz A., Faucher-Giguère C.-A., Dall'Aglio A., McQuinn M., Fechner C., Zaldarriaga M., Hernquist L., Dutta S., 2010, ApJ, 718, 199
Lynds R., 1971, ApJ, 164, L73
McDonald P., Miralda-Escudé J., Rauch M., Sargent W. L. W., Barlow T. A., Cen R., Ostriker J. P., 2000, ApJ, 543, 1
McDonald P., Miralda-Escudé J., Rauch M., Sargent W. L. W., Barlow T. A., Cen R., 2001, ApJ, 562, 52
McDonald P., Seljak U., Cen R., Bode P., Ostriker J. P., 2005, MNRAS, 360, 1471
McQuinn M., Lidz A., Zaldarriaga M., Hernquist L., Hopkins P. F., Dutta S., Faucher-Giguère C.-A., 2009, ApJ, 694, 842
McQuinn M., Hernquist L., Lidz A., Zaldarriaga M., 2011, MNRAS, 415, 977
Meiksin A. A., 2009, Rev. Mod. Phys., 81, 1405
Miralda-Escude J., Rees M. J., 1993, MNRAS, 260, 617
Mortlock D. J. et al., 2011, Nature, 474, 616
Okamoto T., Gao L., Theuns T., 2008, MNRAS, 390, 920
Peeples M. S., Weinberg D. H., Davé R., Fardal M. A., Katz N., 2010, MNRAS, 404, 1295
Planck Collaboration 2013, preprint (arXiv:e-prints)
Rahmati A., Pawlik A. H., Raičevic M., Schaye J., 2013, MNRAS, 430, 2427
Rauch M., 1998, ARA&A, 36, 267
Ricotti M., Gnedin N. Y., Shull J. M., 2000, ApJ, 534, 41
Rorai A., Hennawi J. F., White M., 2013, ApJ, 775, 81
Rudie G. C., Steidel C. C., Pettini M., 2012, ApJ, 757, L30
Sawala T. et al., 2014, preprint (arXiv:e-prints)
Schaye J., 2001, ApJ, 559, 507
Schaye J., Dalla Vecchia C., 2008, MNRAS, 383, 1210
Schaye J., Theuns T., Leonard A., Efstathiou G., 1999, MNRAS, 310, 57
Schaye J., Theuns T., Rauch M., Efstathiou G., Sargent W. L. W., 2000, MNRAS, 318, 817
Schaye J., Aguirre A., Kim T.-S., Theuns T., Rauch M., Sargent W. L. W., 2003, ApJ, 596, 768
Schaye J. et al., 2010, MNRAS, 402, 1536
Springel V., 2005, MNRAS, 364, 1105
Tepper-García T., Richter P., Schaye J., Booth C. M., Dalla Vecchia C., Theuns T., 2012, MNRAS, 425, 1640
Theuns T., Zaroubi S., 2000, MNRAS, 317, 989
Theuns T., Leonard A., Efstathiou G., Pearce F. R., Thomas P. A., 1998, MNRAS, 301, 478
Theuns T., Schaye J., Haehnelt M. G., 2000, MNRAS, 315, 600
Theuns T., Mo H. J., Schaye J., 2001, MNRAS, 321, 450
Theuns T., Zaroubi S., Kim T.-S., Tzanavaris P., Carswell R. F., 2002a, MNRAS, 332, 367
Theuns T., Schaye J., Zaroubi S., Kim T.-S., Tzanavaris P., Carswell B., 2002b, ApJ, 567, L103
Theuns T., Viel M., Kay S., Schaye J., Carswell R. F., Tzanavaris P., 2002c, ApJ, 578, L5
Viel M., Bolton J. S., Haehnelt M. G., 2009, MNRAS, 399, L39
Viel M., Schaye J., Booth C. M., 2013, MNRAS, 429, 1734
Weinberg D. H., Hernquist L., Katz N. S., Miralda-Escudé J., 1996, in Bremer M. N., Malcolm N., eds, Astrophysics and Space Science Library, Vol. 206, Cold Gas at High Redshift. Kluwer, Dordrecht, p. 93

Weymann R. J., Carswell R. F., Smith M. G., 1981, ARA&A, 19, 41
Wiersma R. P. C., Schaye J., Smith B. D., 2009a, MNRAS, 393, 99
Wiersma R. P. C., Schaye J., Theuns T., Dalla Vecchia C., Tornatore L., 2009b, MNRAS, 399, 574
Wiersma R. P. C., Schaye J., Dalla Vecchia C., Booth C. M., Theuns T., Aguirre A., 2010, MNRAS, 409, 132
Wiersma R. P. C., Schaye J., Theuns T., 2011, MNRAS, 415, 353
Zaldarriaga M., Hui L., Tegmark M., 2001, ApJ, 557, 519

APPENDIX A: BIASES IN THE $N_{\rm H\,I}$–Δ RELATION

In Fig. A1, we plot Δ–$N_{\rm H\,I}$ for lines, with $N_{\rm H\,I}$ computed from equation (19), and individual lines coloured with the value of the
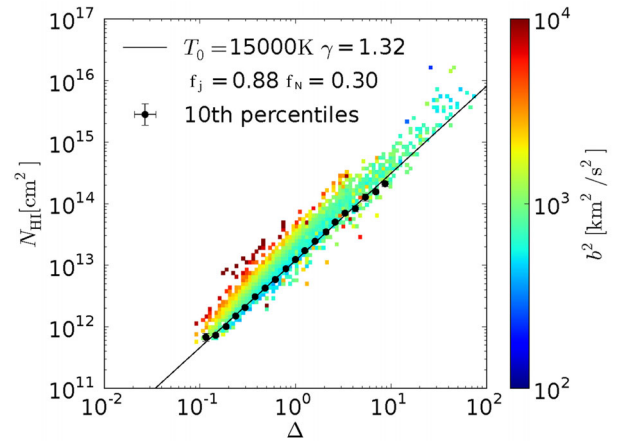

Figure A1. Density contrast – column density Δ–$N_{\rm H\,I}$ relation for lines from the REFERENCE model, coloured according to their line width, b; black dots denote the 10th percentile lowest value of column density at given density contrast. Line width b and column density $N_{\rm H\,I}$ are calculated from equations (18)–(19), respectively. The solid black line is the analytic relation from equation (23). At given Δ, broader lines have higher column density, illustrating that line width biases the column density associated with a given density contrast.
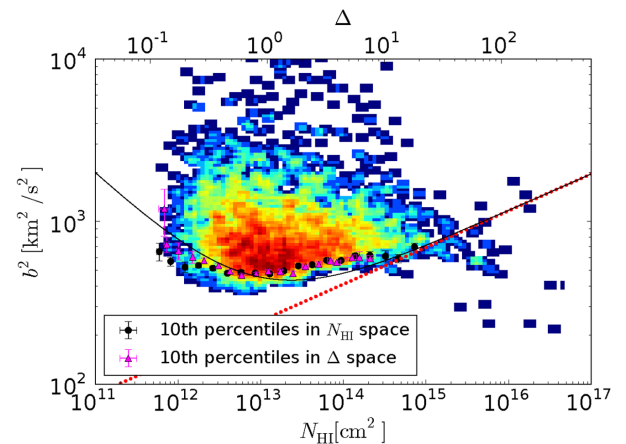

Figure A2. Column density line width $N_{\rm H\,I}$–b relation for the REFERENCE model, colours are a measure of the density of points in the plot; the black line is the model illustrated in Fig. 8; the dotted red line is the thermal width. Black dots denote the 10th percentile lowest values of b for bins in column density, magenta triangles denote the 10th percentile lowest values of b for bins in density contrast Δ, using equation (23) to convert Δ to $N_{\rm H\,I}$. The bias that line width introduces in this relation causes the black dots and red dots to diverge at low $N_{\rm H\,I}$.
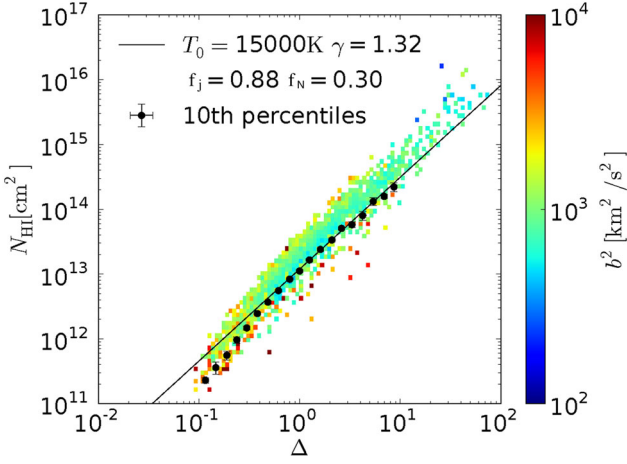
Figure A3. Same as Fig. A1, but with $N_{\mathrm{H\,I}}$ computed from equation (A1). For the low-density lines, the neutral hydrogen column density deviates from equation (23) due to the blending of the faint lines.
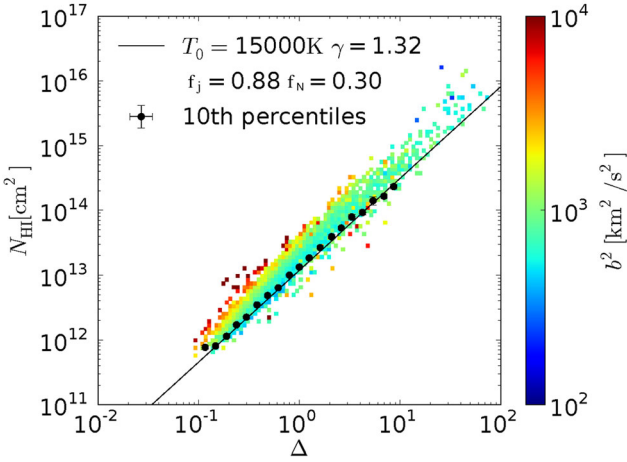

Figure A4. Same as Figs A1 and A3, but with $N_{\mathrm{H\,I}}$ computed from equation (A2). The distribution $\Delta - N_{\mathrm{H\,I}}$ looks similar to the one shown in Fig. A1.

broadening b, calculated from equation (18). Line width biases the value of column density, in the sense that the analytic model of equation (23) (black line in the figure) yields lower values of $N_{\mathrm{H\,I}}$ than equation (19) for broad lines. The effect of this bias on the $N_{\mathrm{H\,I}}$–b relation is illustrated in Fig. A2. Our model for line broadening (black line) works better when lines are characterized by their density contrast (red dots) than by column density (black dots), especially for weak lines. This is because relation equation (23) is fitted to narrower lines.

Here, we also show that equation (19) is equivalent to computing $N_{\mathrm{H\,I}}$ with the integral of the optical depth, as it is often done in the literature. In Fig. A3, we show $\Delta - N_{\mathrm{H\,I}}$, with $N_{\mathrm{H\,I}}$ computed from

$$N_{\mathrm{H\,I}} = \frac{1}{\sigma_0 c} \int_{v_1}^{v_2} \tau \, dv \,, \tag{A1}$$

where v_1 and v_2 are the extremes of the line. If we compare Fig. A3 with Fig. A1, we can see that equation (A1) underestimates the neutral hydrogen column density for the low-density lines.

When lines are blended, the column density computed from equation (A1) may become smaller and smaller as a shorter velocity interval is associated with the line (i.e. when $v_1 \approx v_2$). We can estimate the contribution of these wings, and compute a corrected column density

$$N_{\mathrm{H\,I}} = \frac{1}{\sigma_0 c} \int_{-\infty}^{\infty} \tau \, dv \,, \tag{A2}$$

by extrapolating a Gaussian fit to the line. Such an extrapolated density is closer to what is done in Voigt-profile fitting. Using equation (A2) results in a $b - N_{\mathrm{H\,I}}$ distribution which is very similar from that obtained in Fig. A1, as shown in Fig. A4.

APPENDIX B: DETERMINATION OF f_{J}

In this appendix, we illustrate that our estimate for the extent of absorbers in real space indeed is a good approximation for their actual size. We begin by neglecting peculiar velocities (i.e. generate mock spectra *after* zeroing all peculiar velocities), so that we can unambiguously identify the real-space density structure that gives rise to a given line; we demonstrated in the main text that peculiar velocities have little impact on line widths. Often individual absorption lines correspond to more than one density peak. Such
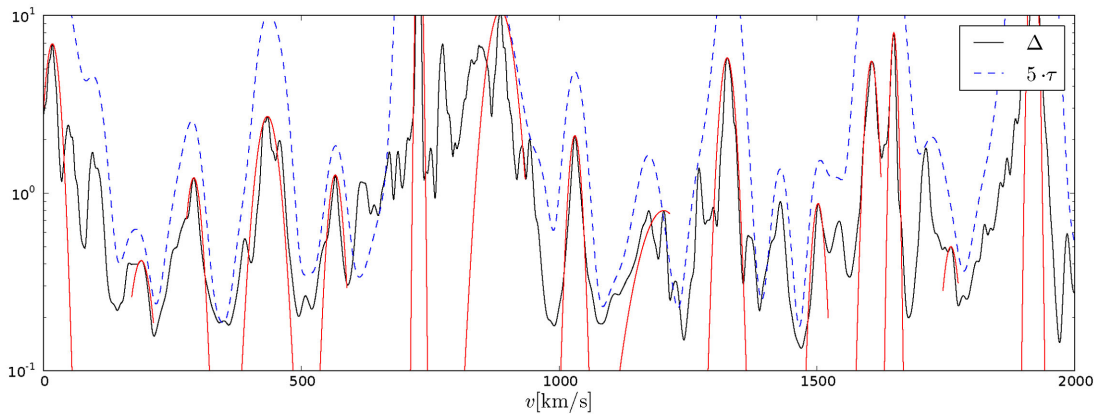
Figure B1. Density profile of absorbers in the absence of peculiar velocities (*black line*) for a mock spectrum calculated from the REFERENCE model; dashed blue line is the scaled optical depth for comparison. Red lines are Gaussian profiles from equation (10), where the width is such that the integral of the density profile of the Gaussian is the same as the one of the multipeaked absorber. The widths of the red Gaussians are often a good approximation to the extent of an absorber.

clustering of peaks sometimes gives rise to very wide lines, as we argued in the text.

In Fig. B1, we show how we have computed the broadening b_Δ in Fig. 3 from the density profile of the multipeaked absorber. The red lines are Gaussian profiles as in equation (10), with v_0 and ρ_0, respectively, the velocity and the density of the local maximum in optical depth. The width b_Δ is such that the integral of the Gaussian density profile is the same as the integral of the density profile of the absorbers. Even though there is often no unique way of associating a 'size' with such complex absorbers, we believe b_Δ is often a good approximation of the extent over which the density contrast of an absorber is significant.

APPENDIX C: DEGENERACY OF PARAMETERS IN THE LINE BROADENING RELATION

For completeness, we illustrate the sensitivity of equation (17) to changes in the $T-\Delta$ relation (varying T_0 and γ; Fig. C1), and varying the fitting parameters f_J and f_N (Fig. C2)

Figure C2. Same as Fig. 8. The dashed (dash–dotted) lines are the model from equation (25) with f_J (f_N) changed by ± 10 per cent.
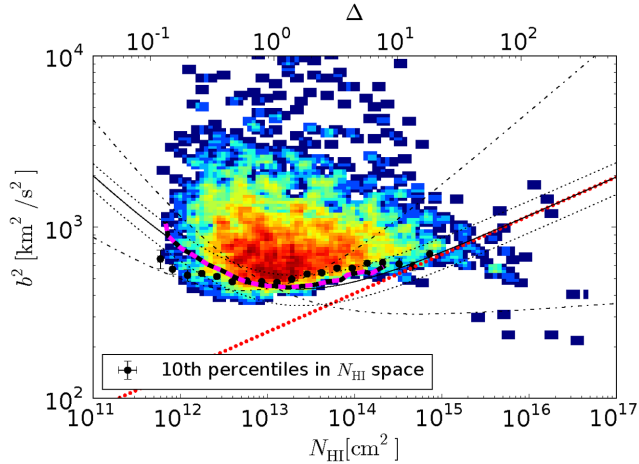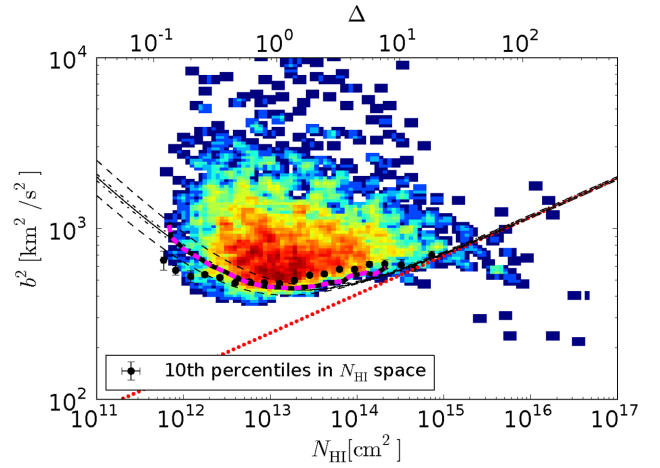

Figure C1. Same as Fig. 8. The dashed (dash–dotted) lines are the model from equation (25) with T_0 (γ) changed by ± 20 per cent.

This paper has been typeset from a TEX/LATEX file prepared by the author.